JOURNAL OF PROPULSION AND POWER
Vol. 34, No. 4, July–August 2018

Agglomerate Sizing in Aluminized Propellants Using Digital Inline Holography and Traditional Diagnostics

Michael S. Powell,* Ibrahim W. Gunduz,† Weixiao Shang,* Jun Chen,‡ and Steven F. Son§
Purdue University, West Lafayette, Indiana 47907
and
Yi Chen¶ and Daniel R. Guildenbecher**
Sandia National Laboratories, Albuquerque, New Mexico 87185

DOI: 10.2514/1.B36859

Aluminized ammonium perchlorate composite propellants can form large molten agglomerated particles that may result in poor combustion performance, slag accumulation, and increased two-phase flow losses. Quantifying agglomerate size distributions are needed to gain an understanding of agglomeration dynamics and ultimately design new propellants for improved performance. Due to complexities of the reacting multiphase environment, agglomerate size diagnostics are difficult and measurement accuracies are poorly understood. To address this, the current work compares three agglomerate sizing techniques applied to two propellant formulations. Particle collection on a quench plate and backlit videography are two relatively common techniques, whereas digital inline holography is an emerging alternative for three-dimensional measurements. Atmospheric pressure combustion results show that all three techniques are able to capture the qualitative trends; however, significant differences exist in the quantitative size distributions and mean diameters. For digital inline holography, methods are proposed that combine temporally resolved high-speed recording with lower-speed but higher spatial resolution measurements to correct for size–velocity correlation biases while extending the measurable size dynamic range. The results from this work provide new guidance for improved agglomerate size measurements along with statistically resolved datasets for validation of agglomerate models.

I. Introduction

COMBUSTION of aluminized ammonium perchlorate (AP) composite propellants can lead to the formation of large molten aluminum (Al) agglomerates, which are ejected into the product gases and contribute to degradation of rocket motor performance via incomplete combustion, slag accumulation, and two-phase flow losses [1–3]. Typically, these effects are more pronounced as the agglomerate diameters increase. For example, momentum and thermal disequilibrium between the condensed and gaseous products, collectively known as two-phase flow losses, are more significant for larger product particles or droplets [3–10]. Although agglomerate sizes can be reduced by decreasing the size of the initial Al powder, this is not without limitations. For example, the use of nanoscale powders has recently been considered [7,9–11]. However, nanoscale Al is high cost, typically contains a large amount of oxide weight (greater than 20 wt. %), and results in poor rheology of the propellant grains due to the high specific surface area [7,9–11]. In addition, slag buildup in the rocket motor is of concern because of higher inert content [2]. As a result, it appears that agglomeration effects cannot be completely eliminated in aluminized solid rocket propellants. Rather, a detailed study of the agglomeration phenomena is needed for prediction and improvement of the rocket motor performance.

Aluminum agglomeration occurs, in large part, due to the difference in the ignition temperature and melting temperature of Al particles [2,3,12]. Before ignition, multiple Al particles tend to melt and coalesce on the propellant surface as a result of heat conduction from the propellant flame, forming larger spherical droplets via surface tension. Binder and AP decomposition evolve gases that induce drag forces on the molten droplets, which are eventually ejected from the propellant surface. Local hot zones due to AP diffusion flames may ignite the molten droplets, leading to visible flame zones, particularly around the largest agglomerates. An example is shown in Fig. 1, taken from the experimental videography results discussed later in this work.

The size distribution of Al agglomerates is one of the most important predictors of performance effects. This has motivated the generation of a number of models to predict agglomerate size distributions based on the initial Al, AP, and binder characteristics [5,13–15]. Validation of such models requires accurate measurement of Al agglomerates with defined uncertainties applied to propellants of known composition. Unfortunately, due to the complexity of the measurements, few literature results contained quantified uncertainties. Furthermore, many Al agglomerate distributions provided in the literature were obtained for propellant compositions that were either poorly defined or not publically available. Motivated by this, the current work investigates measurement accuracies by experimentally considering multiple particle sizing techniques applied to propellants with well-defined compositions.

Experimental techniques for sizing Al agglomerations included phase Doppler anemometry [16], laser diffraction [17], particle collection [1,4,7,9,10,18,19], videography [1,12,20,21], schlieren [22], shadowgraphy [20], holography [16,23–26], and digital inline holography (DIH) [27–29]. Particle collection has been performed, both near the burning surface and far downstream with either solid quenching media or liquid quench baths [1,4,9,10,18]. Agglomerate sizes were found to be larger than the initial Al additives [1,4,9,10] and tended to decrease as the operating pressure increased [4,18,30–32]. Although particle collection was relatively straightforward, it was intrusive in nature and might introduce bias into

Received 16 August 2017; revision received 29 November 2017; accepted for publication 18 January 2018; published online 13 April 2018.

*Graduate Student, School of Mechanical Engineering, 500 Allison Road.
†Research Assistant Professor, School of Mechanical Engineering, 500 Allison Road.
‡Associate Professor, School of Mechanical Engineering, 500 Allison Road.
§Professor, School of Mechanical Engineering, 500 Allison Road. Senior Member AIAA.
¶Postdoctoral Appointee, Engineering Sciences Center, P.O. Box 5800, Mail Stop 0828. Member AIAA.
**Principle Member of the Technical Staff, Engineering Sciences Center, P.O. Box 5800, Mail Stop 0840. Senior Member AIAA.

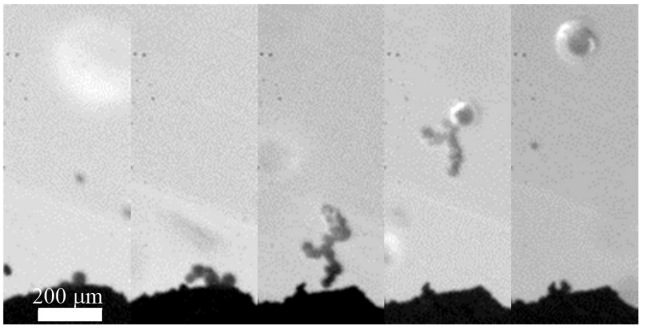

Fig. 1 Typical agglomeration dynamics in aluminized propellants.

measurements because the quench media directly interfered with the dynamics of the gas phase. Furthermore, particles might be subject to flattening as they are forced to a sudden stop on the quench media, leading to inaccurate sizing of the two-dimensional area.

Direct microscopic videography of the agglomerates evolved from a burning propellant sample has also been used for sizing. As with particle collection, a nontrivial amount of agglomerates was found to be much larger than the initial Al particle size [1,20,21]. This technique is relatively simple and nonintrusive, although some difficulty arises from high intensity of the burning Al that may saturate the imaging system [1,21,31,33]. The optical density of the alumina smoke and other combustion products also causes issues, especially at higher pressures [1,21,31]. Unfortunately, only particles that are in the narrow focal plane can be imaged and sized using this technique, so each video frame provides relatively few particles. Therefore, in many cases, numerous experiments are required to obtain statistically significant datasets.

Finally, holographic techniques have also been applied to propellant combustion to record holograms of Al agglomerations [23–29]. Briefly, holography uses the interference between two light waves to record diffraction patterns that can be reconstructed to produce a three-dimensional (3-D) image [34–36]. As with other techniques, a significant portion of the agglomerates was found to be larger than initial constituents, but there was noteworthy obfuscation from alumina smoke when recording holograms at higher pressures [24–26]. Three-dimensional reconstruction allowed for a greater number of particles to be viewed and sized from each image such that fewer experiments were needed compared to videography. Recorded holograms were originally imaged onto plates, leading to only one hologram per experiment [23–26]. More recently, temporal resolution has been enabled with digital recording [27–29].

In the following, experiments are conducted with particle collection, videography, and DIH. Comparison of the three techniques increases the overall confidence in the individual measurements and allows for improved understanding of uncertainties and biases. Particular emphasis is placed on DIH, which has recently been demonstrated for rapid statistical quantification [27–29] but, as an emerging technique, has yet to be fully validated. The work begins with a discussion of the propellant formulations and experimental configurations. Following this, data processing methods are detailed, and new techniques are proposed for correcting size–velocity correlation biases from imaging results. Finally, measured particle size distributions are compared for two different propellant formulations. The results provide additional guidance for characterization of agglomerates and further develop techniques for rapid and accurate evaluation of novel propellant formulations.

II. Experimental Methods

Two propellant formulations were prepared using methods reported in previous works [9,10]. One propellant contained initially spherical Al particles (Valimet H30), whereas the other used Al particles with a nonspherical, flakelike morphology (Poudres Hermillon YX-49). Each of the powders was sieved between −200 and +500 mesh sieves to the size range of 25–75 μm. Sieved particle size distributions were measured and are available in [10]. In both propellants, 71% of the total weight consisted of a bimodal distribution of ammonium perchlorate with a 4:1 coarse-to-fine ratio and average AP diameters of 200 and 20 μm (ATK), respectively. An additional 15% of the solid loading by weight was aluminum powder (flake or spherical), resulting in a solids loading of 86%. The binder consisted of 10.53% R45M hydroxyl-terminated polybutadiene (Firefox Enterprises), 0.20% Tepanol HX-878 (3M Corp.), 2.11% isodecyl pelargonate (RCS Rocket Motor Components, Inc.), and 1.16% isophorone diisocyanate (Firefox Enterprises) of the total propellant weight. Components were mixed in stages, initially by hand, for 5 min intervals; and then with a LabRAM resonant mixer (Resodyn) operated at 90% intensity for 5 min. Samples were held at a vacuum of less than 35 mbar for 10 min to remove air bubbles. Propellant was then packed into 6.75-mm-diam strands measuring ∼60 mm in length. Strands were cured in a convection oven at 60°C for seven days. In an experiment, propellant samples were sectioned to 15 mm in length, placed into a test fixture, and ignited. The top-burning experiments were conducted at room temperature and at atmospheric pressure.

High-speed videography of the resulting propellant burns was recorded with a Vision Research Phantom V7.3 camera operated at 5000 frames per second and 1 μs exposure with a window of 400 × 300 pixels giving 1.5 s of video. Approximately 4× magnification was achieved with a long-distance microscope (Infinity K2 with CF2 objective). The internal aperture of the K2 lens was set at the minimum opening to cut down the intense broadband emission from burning agglomerates and to increase the depth of field. A focused green light-emitting diode (LED) was used for backlighting, and a 532 nm optical bandpass filter with 20 nm full width at half-maximum (FWHM) was used to reduce broadband emission from the Al particles while capturing most of the light from the green LED. The spatial resolution was measured to be 5.49 μm/pixel when the sample was at the shortest working distance allowed by the lens (∼120 mm). Particles were measured from the surface up to ∼3 mm above the propellant. As will be discussed further in the next section, particle sizes were analyzed using a custom MATLAB-based image-processing routine.

Particle collection was performed in a separate test using an apparatus reported previously for high-pressure experiments inside of a combustion vessel [9,10] and modified here to work in open atmosphere. The propellant sample was used as a beam block for a 10 mW helium–neon laser until the burning surface recessed below the laser level. Impingement of the laser onto a photodiode triggered a circuit to reverse the polarity of a dc motor, allowing a collection plate to swing through the propellant plume and collect quenched particles. Sampling was performed at a height ∼2–6 mm above the propellant surface at a transverse speed of ∼7 m/s onto borosilicate quench disks (McMaster Carr 8477K18). After an experiment, the samples were imaged using a MX (G)-10C lens on a Hirox digital microscope with an OL-140 II adapter. Using this lens and adapter combination, a pixel pitch of ∼1.4 μm/pixel was achieved. Finally, these images were processed to segment and quantify individual particles. Once again, further details will be provided in the subsequent section.

Previously, the DIH of propellants has been performed with high-resolution low-speed imaging configurations for which the record rates were on the order of a few hertz [28,29] and high-speed lower-resolution configurations with record rates on the order of kilohertz [27]. As will be discussed later in this work, these two methods may be subjected to specific biases. To quantify these effects, this work uniquely employed a two-view configuration with both high-speed and low-speed recordings, as shown in Fig. 2. The fields of view, pixel pitches, and frame rates were 4000 × 2700 and 800 × 600 pixels^2, 2.1 and 5.3 μm/pixel, and 4 and 4000 Hz, respectively. The high-speed videos used a Phantom V7.3 camera (∼1 μs exposure), and the low-speed data used an IMPERX ICL-B4020M camera (∼10 μs exposure). Particles from 0 mm up to ∼6 mm above the burning surface were measured from the fields of view during the short data acquisition times. A double-pulsed 532 nm Nd:YAG laser (New Wave Solo PIV laser) was implemented as the illumination source for the low-speed view, whereas a low-powered continuous-wave Nd:YAG, 532 nm laser was implemented for the high-speed view. The initial ∼3 mm-diam beams

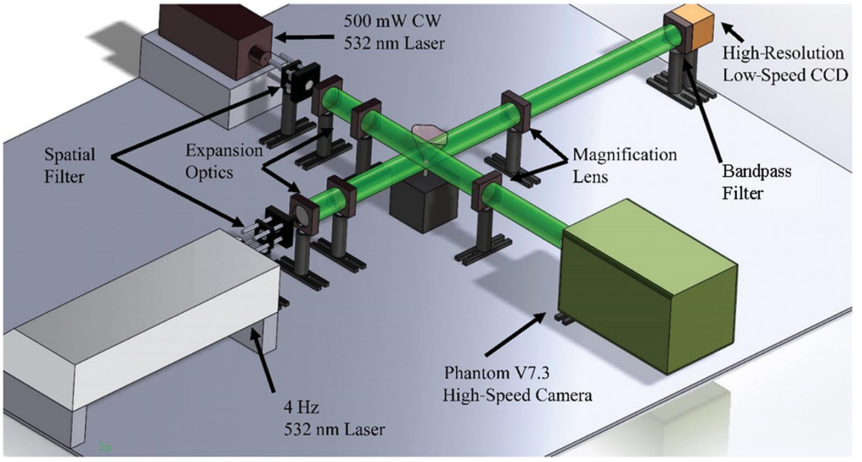

Fig. 2 Experimental configuration for the transverse DIH experiment. CCD, charge-coupled device, CW, continuous wave.

for both views were spatially filtered before expansion to a final diameter of ~50 mm. A 532 nm bandpass filter with ±1.0 nm FWHM was affixed to each camera to block extraneous light from the burning propellant. Finally, reconstruction of holograms, sizing, and velocity measurements were completed at Sandia National Laboratories, with details again given in the next section.

For all the measurement methods, particle diameters are obtained by quantifying the number of pixels in a silhouetted area and converting the value to an area-equivalent circular diameter. For nonspherical clumpy or coral-shaped particles, the projected area-equivalent diameters will tend to be higher than their underlying volume-equivalent diameters. However, because all of the measurement techniques in this work use projected area for sizing, they should share this same bias if nonspherical particles are encountered. In this situation, the diameter values that are obtained should be readily comparable.

III. Results

A. Digital Inline Holography

Select raw frames from digital in-line holography of the baseline spherical Al propellant are shown in the top row of Fig. 3. Figure 3a shows one image from a 4 Hz recording, whereas Fig. 3b shows a few frames from a 4000 Hz recording. Both results clearly show diffraction patterns that originate from the particles in the flow as well as the portion of the burning surface within the field of view.

As discussed in detail elsewhere [35,36], DIH images can be numerically refocused via application of the diffraction integral equation. This essentially treats each pixel in the hologram plane as the origin of a spherical wave. All waves from every pixel are then numerically propagated to the output plane at optical depth z and convolved together to form a refocused image. As such, the refocusing of DIH images can be understood as a discrete realization of the Huygens–Fresnel principle and is illustrated in the bottom row of Fig. 3, where each image has been numerically refocused to the approximate optical depth of the burning surface ($z = 24.8$ mm for the 4 Hz results in Fig. 3a, and $z = 10.5$ mm for the 4000 Hz results in Fig. 3b). At this optical depth, many in-focus particles are observed, whereas a number of other features remain out of focus and are therefore contained at other optical depths.

The in-focus depths of all particles are automatically located using the methods detailed in [27–29,37–39] and briefly reviewed here. First, the hybrid object localization method, as discussed in [36,37], is used to determine initial estimates for the x, y location and in-plane

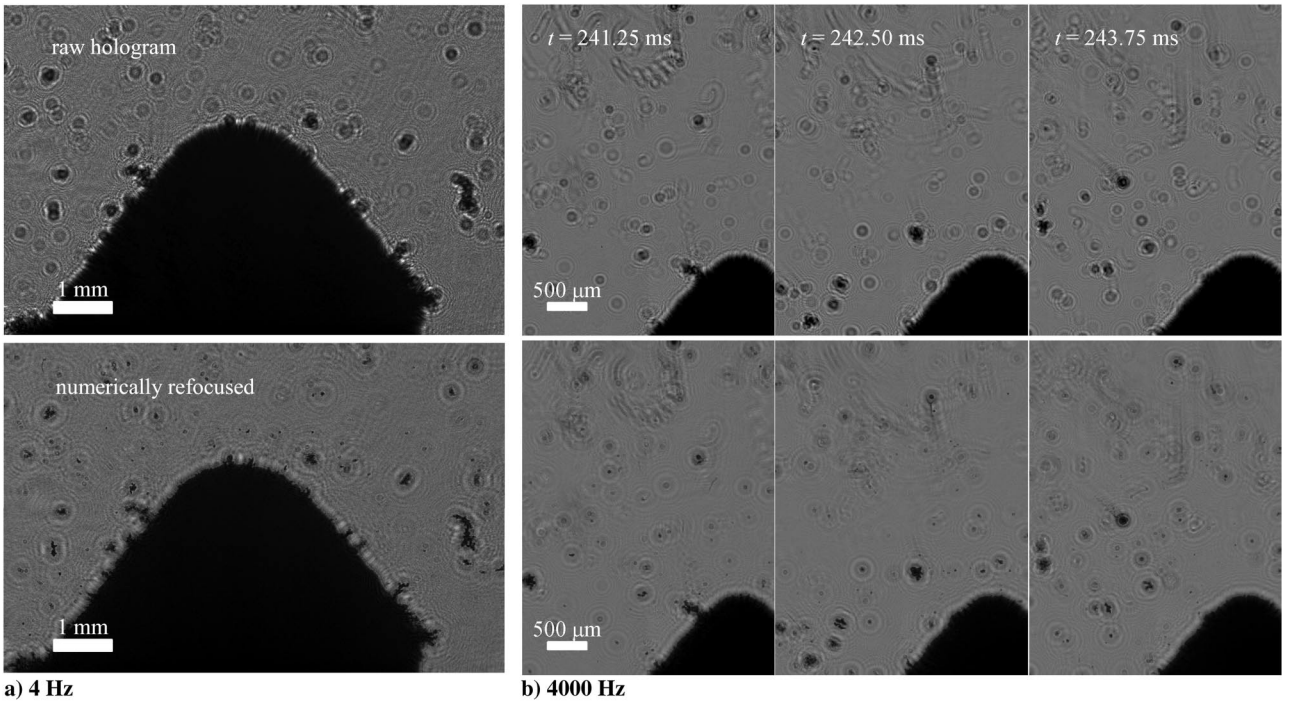

a) 4 Hz **b) 4000 Hz**

Fig. 3 Digital inline holography of spherical Al propellant recorded at a) 4 Hz and b) 4000 Hz.

diameter of each particle within the field of view. From this, subwindows are defined around each initial particle estimate. Then, the hologram is refocused to 2001 planes between $z = 0$ to $z = 50$ mm. Using the methods discussed in [39], a sharpness metric is determined within each subwindow for each z plane. Finally, the optimal z location of each particle is determined by the z plane, where the sharpness metric is maximum. Once all particle x, y, and z locations are determined in this manner, particle morphologies are extracted by once again applying the hybrid method [37] to the refocused particle images at their measured z locations. The typical accuracy of the DIH diameter estimates using the hybrid method is on the order 1 to 7%, depending on particle size [38].

Figure 4 summarizes the results measured from the 4 Hz hologram image shown in Fig. 3a. Here, bright squares show the particle images refocused to the measured optical depth of each particle. Outlines show the measured in-plane particle morphologies colored by their area-equivalent diameter. Due to the high temperatures of aluminized propellant flames [28] and the pyrolysis temperatures of the binder [40], it can be assumed that the large nonspherical particles represent aluminum agglomerates that have not fully sintered into spheres due to their aluminum oxide coatings. Finally, the background shows the refocused image corresponding to the bottom row in Fig. 3a.

Individual frames from the 4000 Hz recording are also processed in this same manner. In addition, the temporal resolution is sufficient such that individual particles can be tracked over multiple frames as they traverse through the field of view. A regression-based multiframe tracking (RMT) algorithm as detailed in [27] is briefly summarized here. First, nearest neighbor matching is used to estimate particle trajectories from one frame to the next. Following this, individual x–y trajectories are fit to quadratic functions with respect to time. This allows the results to be extrapolated in time such that similar trajectories can be linked together, unmatched particles added, and outliers removed. Next, the process is repeated in an iterative fashion until no further particle trajectories can be located that satisfy user-defined acceptance criteria. Finally, to account for the inherently higher positional uncertainty in the optical depth direction [35], particle z trajectories are estimated using a linear fit to the measured z positions with respect to time. If completely successful, this measurement assigns a single trajectory to every particle that passes through the field of view. From this, a mean diameter and velocity can be measured for each particle.

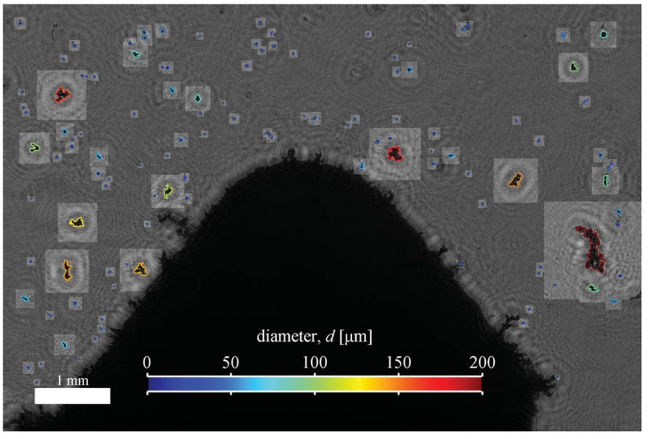

Fig. 4 Spatially resolved 4 Hz DIH results from the spherical Al image shown in Fig. 3a.

Figure 5 shows select frames from a 4000 Hz recording of the spherical Al propellant corresponding to the images in Fig. 3b. Data are presented similarly to Fig. 4, with the addition of the velocity vectors shown in white.

Compared to the 4 Hz results in Fig. 4, the 4000 Hz, temporally resolved data in Fig. 5 clearly have a lower rate of successful particle detection. This may be attributed to a number of factors. The high-speed camera used to record Fig. 5 has a smaller bit depth and probably a higher noise floor as compared to the 4 Hz imager. This likely contributes to an increased rate of particle rejection during the initial image processing. Furthermore, the high-speed camera is discretized into fewer and larger pixels. During image processing, regions are rejected when the measured diameter is less than three effective pixels. This corresponds to minimum detectable diameters of 6.3 and 15.9 μm for the 4 and 4000 Hz recordings, respectively. Consequently, the 4000 Hz recording is likely unable to measure a significant portion of the smallest particles in the flow. Finally, application of the RMT technique also acts as a filter that rejects particles that cannot be linked to other measured particles over time. All of these effects likely combine together to produce the decreased particle detection efficiency seen in Fig. 5.

DIH of the flake Al propellant was also performed and processed as described previously. Figure 6 shows typical results. Similar to the spherical Al results, the 4 Hz DIH results for flake Al in Fig. 6a appear to accurately quantify a vast majority of the particles visible within the field of view, whereas the 4000 Hz results in Fig. 6b provide temporal resolution but at the cost of reduced particle detection efficiency, due to the same reasons as before for the spherical Al propellant.

When comparing the initial flake Al in Fig. 6a with the initial spherical Al in Fig. 4, it is clear that the final flake Al agglomerates appear to be larger and more spherical. In addition, more long streaks, which denote hotter aluminum combustion flame zones, are visible [28]. Thus, it is reasonable to conclude that the initial flake Al particles have melted their aluminum oxide shells in order to form sintered spherical ball-like agglomerates. On the other hand, the aluminum oxide shells of the particles in the initial spherical Al propellant appear to prevent the formation of larger ball-like

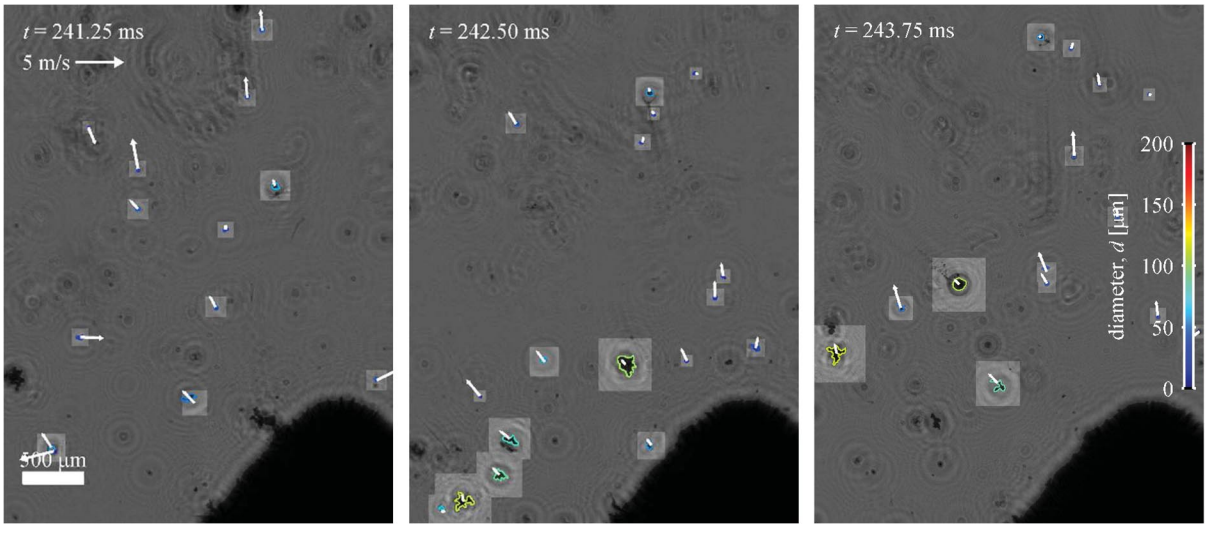

Fig. 5 Temporally resolved 4000 Hz DIH results from spherical Al images shown in Fig. 3b.

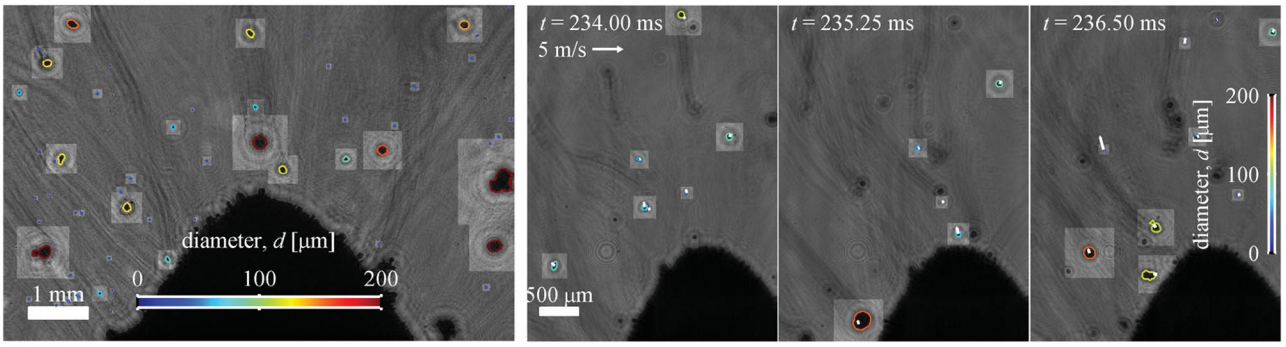

a) 4 Hz b) 4000 Hz

Fig. 6 Digital inline holography of flake Al propellant recorded at a) 4 Hz and b) 4000 Hz.

agglomerates near the propellant surface. These morphology results are consistent with previous imaging data for these propellants [9].

For both the spherical and flake propellants, experiments were performed multiple times in order to quantify a large number of particles and gather accurate statistics. For the spherical Al propellant, 52 and 11 strand burns were recorded with the 4 and 4000 Hz configuration, respectively. In total, 30,799 particles were quantified from all 4 Hz recordings, which was an average of 592 particles per burn. In comparison, the 4000 Hz recordings resulted in 72,087 total measured particles, which were an average of 6553 particles per burn. Likewise, for the flake Al propellant, 22 and 16 strand burns were recorded with the 4 and 4000 Hz configurations, respectively. In total, 2982 particles were quantified from all 4 Hz recordings, which were an average of 136 particles per burn. In comparison, the 4000 Hz recordings resulted in 30,963 total measured particles, which was an average of 1935 particles per burn.

Figure 7 compares the measured particle size distributions. For reasons that will become apparent in the discussion that follows, results from the 4 Hz DIH are referred to as spatially resolved; whereas the 4000 Hz DIH is referred to as temporally resolved. The top row shows the probability density by count, where each bar is determined by the total number of particles for which the measured diameter is within the bin range and normalized such that the integral of the probability density is one. The bottom row shows the probability density by volume, where each bar is determined by the total number of particles for which the measured diameter is within the bin range multiplied by the mean volume of particles within that bin and again normalized such that the integral of the probability density is equal to one. The error bars are calculated by assuming a Poisson distribution in the probability of collecting particles within a particular bin interval. This error is then propagated through the calculation of the volume probability density.

A comparison of the 4 Hz spatially resolved probability densities with the 4000 Hz temporally resolved data in Fig. 7 reveals a few trends. The dotted green line in this figure represents the minimum measurable diameter for the 4000 Hz DIH. The temporally resolved data, in red, consistently show higher probabilities at larger diameters. The 4 Hz spatially resolved data, in blue, have a higher size-dynamic range and quantify a significant number of particles at diameters smaller than the size-dynamic range of the 4000 Hz temporally resolved data. Likely due to this, the normalized probability densities by count from the 4000 Hz results display higher probabilities within the size range to the right of the dotted line.

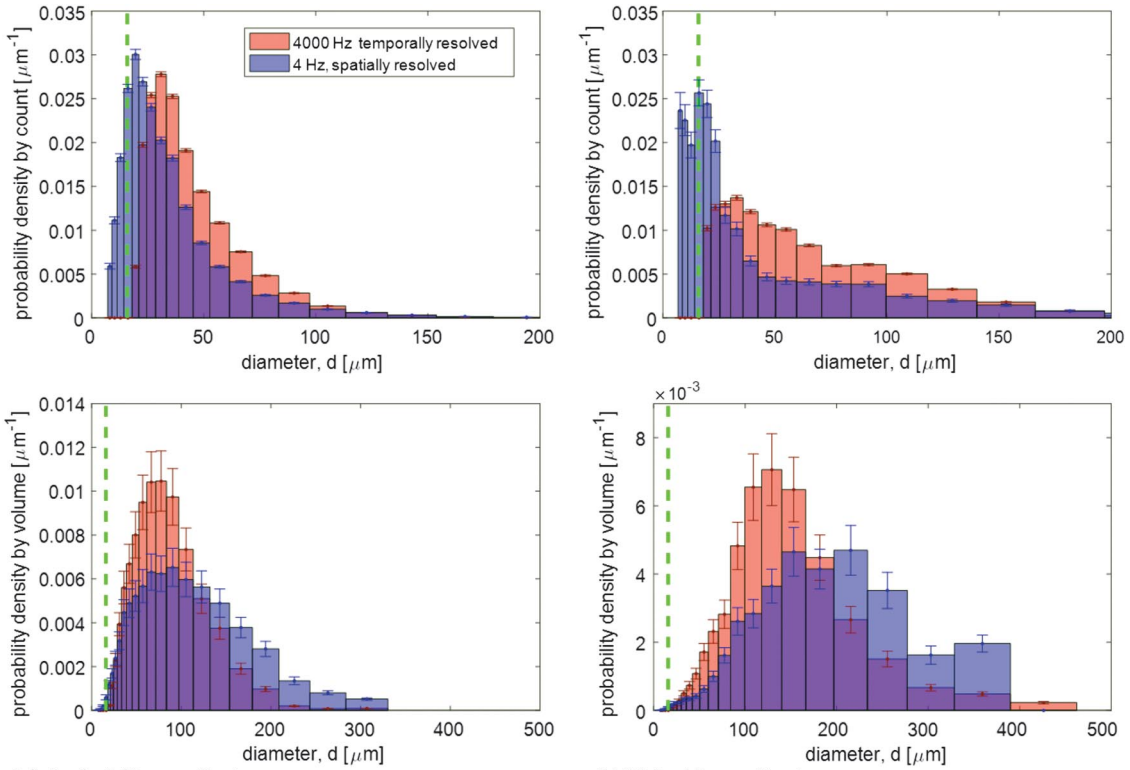

a) Spherical Al propellant b) Flake Al propellant

Fig. 7 Probability densities quantified by DIH.

Trends observed in the probability densities weighted by volume in the bottom row are perhaps more interesting. The spatially resolved data consistently show higher probabilities at larger diameters. Because the particle volume scales by the diameter cubed, the spatially resolved DIH results indicate that a very small percentage of the total volume is made up of particles below the minimum measurable diameter for the 4000 Hz DIH shown by the dotted green line. This indicates that the observed differences are not likely due to missing information in the temporally resolved probability density below this diameter. Instead, it is proposed that much of the observed differences can be attributed to the well-known effects of size–velocity correlations.

Figure 8 plots the measured particle x–y velocities versus the measured diameter from the 4000 Hz recording. Particles accelerate away from the surface due to aerodynamic drag, and the largest particles tend to accelerate more slowly as compared to the smaller particles. Consequently, the mean particle velocity conditioned on particle diameter, shown by the black squares in Fig. 8, tends to decrease with increasing diameter. Due to their slower velocity, these large particles reside within the measurement volume for longer periods of time.

The 4 Hz DIH recording quantifies all particles within the measurement volume at discrete instants in time and is an example of spatial sampling. In contrast, the inclusion of particle tracking in the 4000 Hz results produces a measure of all of the particles that travel through the fixed measurement volume over time, illustrating an example of temporal sampling. As noted elsewhere [41], a spatially sampled particle size measurement is biased toward those particle size classes that have a longer residence time within the field of view. This phenomenon is likely why the spatially resolved 4 Hz results in the bottom row of Fig. 7 show a higher probability as compared to the temporally sampled 4000 Hz results at large diameters.

Assuming all particles are of the same material, the particle mass flux conditioned on diameter is directly proportional to the temporally sampled probability density weighted by volume. A majority of propellant agglomeration or combustion models either predict particle mass fluxes or use mass fluxes as an input boundary condition [13–15,42]. Therefore, it is this temporally sampled particle size distribution that is typically of most interest.

The spatially resolved 4 Hz probability size distributions can be converted to temporally resolved distributions by multiplying each size class by the inverse of the mean particle residence time [41]. Assuming the extent of the measurement volume is constant for all particle size classes, this is equivalent to multiplying the probability of each particle size class by the mean velocity of the particles in that size class.

To apply this theory to the current results, the measured mean particle size–velocity correlations are first fit to a function of the following form:

$$v_{xy} = A - B\exp(-C/d^2) \tag{1}$$

where A, B, and C are constants. This functional form is derived by integration of the Stokes drag relation over a sphere of diameter d assuming constant gas velocity and viscosity. Next, the spatially sampled particle size distributions in Fig. 7 are multiplied by the mean velocity at each bin as given by the best fit of Eq. (1) shown in Fig. 8. Finally, the probability densities are then renormalized such that their integrals are again equal to one.

The blue curves in Fig. 9 show the result after the 4 Hz data have been corrected for the size–velocity (s-v) biases in this manner. By combining the 4000 Hz high-speed DIH recording to capture the mean size–velocity correlation with the 4 Hz higher-resolution DIH data, which better quantify all particles within the field of view, the end result is a temporally resolved particle size distribution with a size-dynamic range that exceeds what could be achieved with high-speed DIH alone while also reducing the potential biases that arise from the lower successful particle detection rate in high-speed DIH. This paper is believed to be the first time that such a combination of temporally resolved and spatially resolved DIH has been reported in the archival literature.

Finally, assuming that the blue curves in Fig. 9 represents the best measurement of the true temporally resolved particle size distributions, the percentage of particles below the dotted green line can be used to estimate the percentage of particles that are missed from the high-speed recording. With that, the 4000 Hz data in Fig. 9 have been scaled to account for the missing probability of particles below the measurable dynamic range (d-r) of the high-speed recording. The 95% confidence interval of the velocity measurement is then propagated into the error bar estimates to incorporate uncertainties stemming from the size–velocity correction method.

Comparison of the original particle size probability densities in Fig. 7 with the corrected results in Fig. 9 show that the corrections significantly improve the agreement between the two DIH measurements. In [43], simulations were presented that demonstrated that the corrections employed here produce perfect agreement when all other sources of experimental biases are removed. Therefore, the remaining discrepancies in Fig. 9 are likely due to other measurement biases, which have yet to be fully identified. One suspected remaining bias could arise from the limited particle detection efficiency in the 4000 Hz results. It is possible that the data processing methods may be more efficient at detecting and tracking particles in certain size

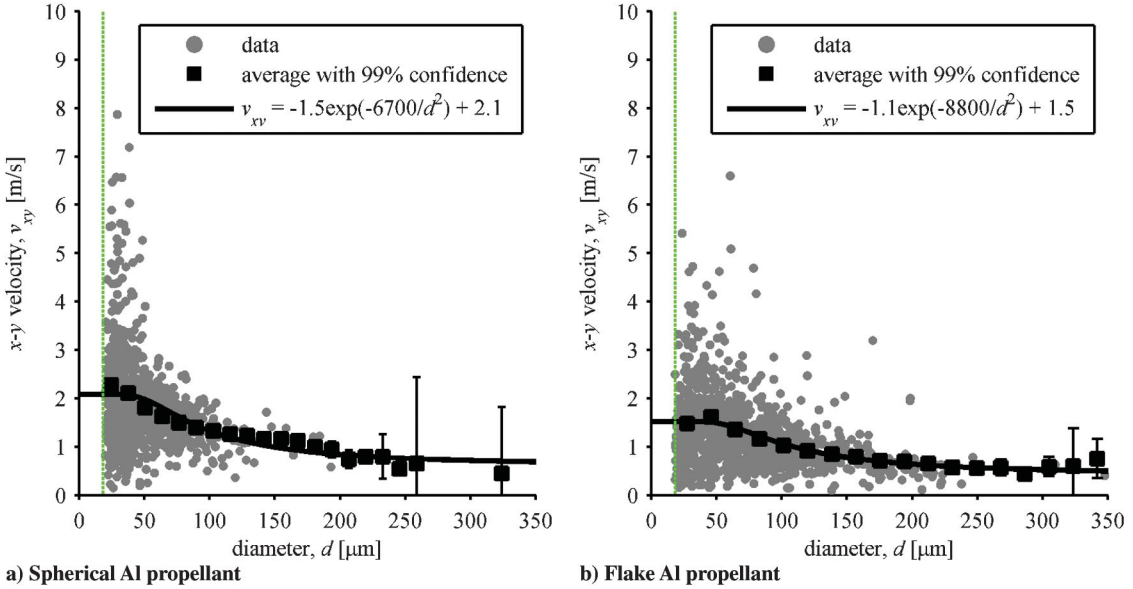

a) Spherical Al propellant **b) Flake Al propellant**

Fig. 8 Size–velocity correlations measured with 4000 Hz DIH.

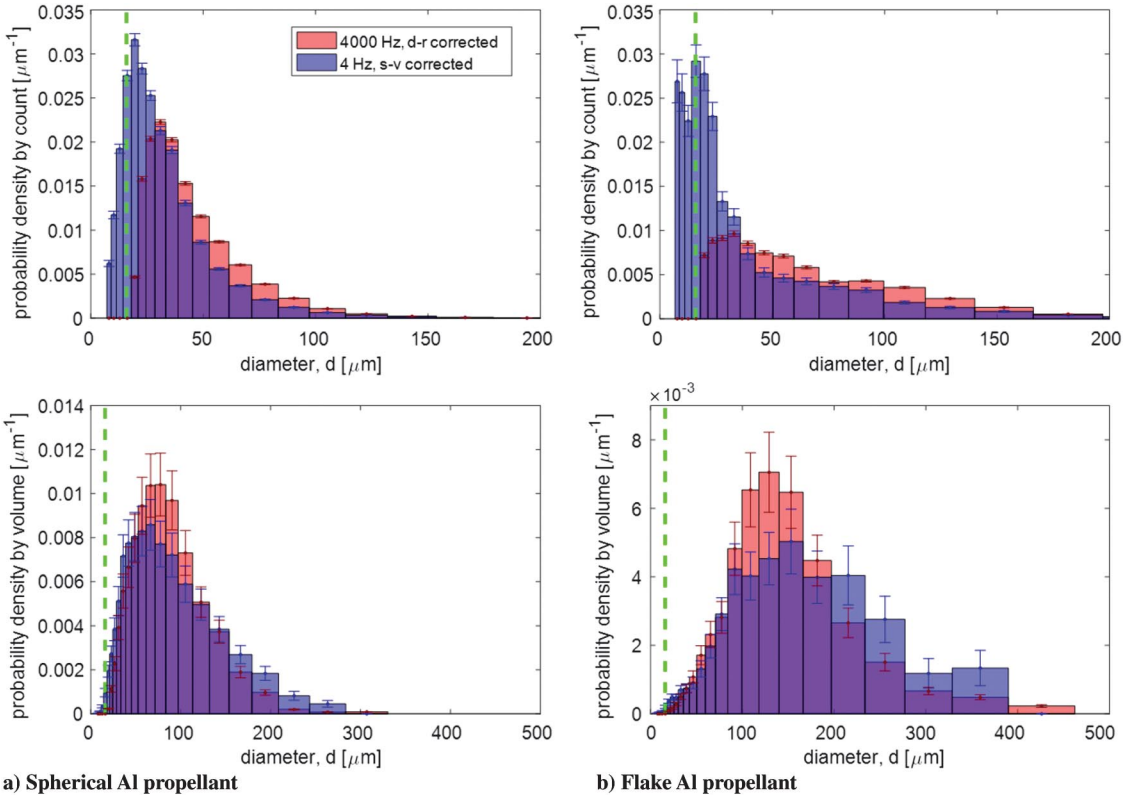

a) Spherical Al propellant b) Flake Al propellant

Fig. 9 Temporally resolved probability densities quantified by DIH.

classes. For example, large and slow particles would be easier to track due to their longer residence times within the field of view. This could be the reason why the probability density by count is higher at larger diameters for the 4000 Hz as compared to the 4 Hz results. More work would be needed to fully explore this and other potential bias sources.

B. Particle Collection

Figure 10 presents typical particle collection results for the spherical Al propellant. Figure 10a is the raw collection plate image, whereas Fig. 10b is the binary contrast of that image. Quenched products for flake Al using particle collection are similar but with noticeably larger agglomerates present on the quench disk. Due to their small size, the molten particles are expected to rapidly quench as they impact on the relatively cold disk. Nevertheless, some morphological changes may occur during the finite quench time, which could be why fewer nonspherical structures are observed in Fig. 10a as compared to the in situ images of Figs. 3–5. The detection of particle regions requires high contrast to distinguish between the collection surface and agglomerates. Assuming reasonable relative contrast of the images, most image-processing software is capable of isolating the particles from the background. Here, ImageJ is used to segment individual particles from the binary contrast image. Particle diameter estimates have an expected error of ~ 3 μm based on the image resolution and the edge detection algorithm. No measured region is accepted with a diameter of less than 6 pixels, which is equivalent to 8.4 μm. This was found to be appropriate to prevent detection regions that were significantly less than the initial size of the unreacted aluminum and might have originated from either alumina smoke or imaging noise. Two strands of propellant were tested for both spherical and flake Al propellants. This yielded $\sim$2000 measured particles, resulting in roughly 1000 particles per burn.

C. Videography

Figure 11 shows a typical image from the high-speed videography of the spherical Al propellant. Particle edges are detected using a Sobel gradient filter in the MATLAB image-processing toolbox. Next, holes within binary regions are filled. Finally, individual regions are segmented to determine their area-equivalent diameter. As is typically done, edge detection parameters are manually selected to attempt to segment only those particles that appear to be in focus.

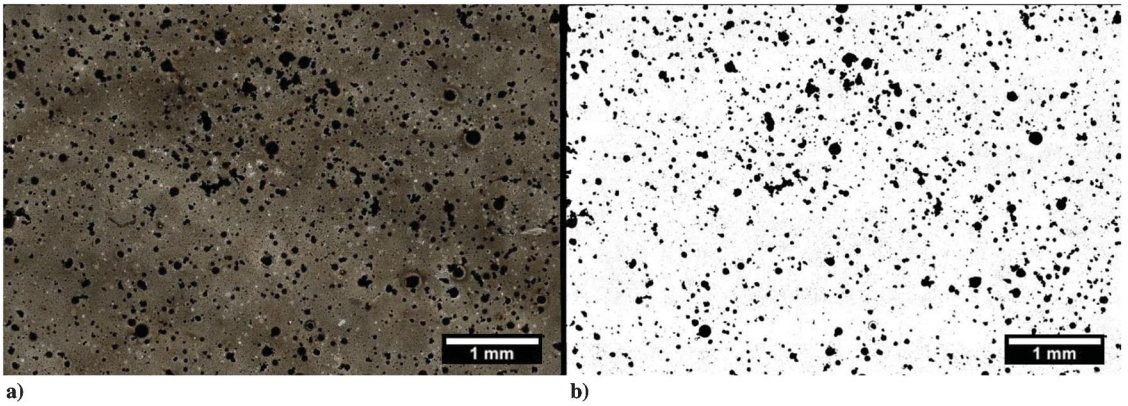

a) b)

Fig. 10 Raw images of a) particle quench disk for spherical Al propellant and b) the binary contrast of Fig. 10a.

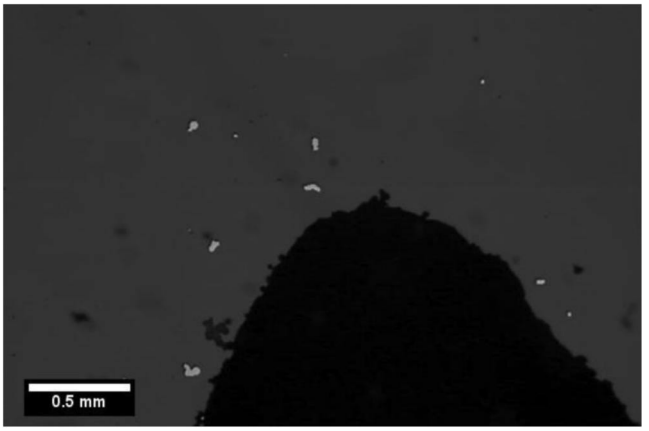

Fig. 11 Still image from videography of spherical Al propellant with measured particle outlines in white.

In addition, no attempt is made to track individual particles over time. Therefore, these results are also subject to size–velocity biases, as discussed previously for the 4 Hz DIH. Diameter estimates are expected to have an accuracy of ~11 μm based on the pixel resolution and the edge detection algorithm. To minimize false detections, no region is accepted with a measured diameter less than three pixels, resulting in a minimum measurable particle diameter of 16.5 μm. Sample totals for videography are ~1000 particles collected from a single burn for both spherical and flake Al propellants. Due to limited quantities of propellant from each batch, additional videography experiments could not be conducted.

IV. Discussion

Figures 12 and 13 compare the probability size distributions measured with DIH, particle collection, and videography. Both figures plot the same DIH results in blue which correspond to the 4 Hz size–velocity corrected results first reported in Fig. 9. For the reasons mentioned in the previous section, this is believed to be the most accurate quantification of the size distribution using DIH.

The results in Figs. 12 and 13 reveal a number of trends. For all measurement techniques, the flake Al agglomerate diameters are significantly larger than the spherical Al propellant. This observation is particularly evident in the volumetrically weighted results in the bottom row of Figs. 12 and 13, where the peak in the probability density is roughly twice as large for the flake Al as compared to the spherical Al. Similar results were obtained using particle collection at higher pressures in [9,10]. Recall that the initial flake and spherical particles in the unburned propellants were sieved to within the same size range [10]. Therefore, the difference in final agglomerate diameters is related to particle agglomeration dynamics on the burning surface. Additional discussions of these dynamics were provided in [9,10]. For rocket motor applications, increased agglomerate sizes can lead to increased two-phase flow losses, slag accumulation, and incomplete combustion. Consequently, it is generally desired to design and test propellants for reduced agglomeration. Results such as those in Figs. 12 and 13 as well as the measurement techniques presented here provide useful metrics on the success of such design efforts.

The main focus of this section is to compare agglomerate measurement techniques. Here, we have attempted to perform each measurement technique in a manner consistent with what is typically done in the literature. Therefore, a comparison of these results may give a general impression of typical levels of accuracies and biases of size distributions reported in the literature. Of course, each technique has many variants, and quantitative details will depend strongly the intricacies of each individual experiment. Overall, the approximate agreement of the results in Figs. 12 and 13 indicates that all three techniques capture the qualitative change in agglomerate probability densities when the propellant material properties are altered from spherical to flake Al. Therefore, any of the three techniques, if carefully executed, is likely sufficient to study qualitative changes in agglomeration dynamics. On the other hand, detailed comparisons of the distributions do indicate some significant differences, which will be discussed further in subsequent paragraphs. Consequently, a derivation of trends by comparing results from different measurement

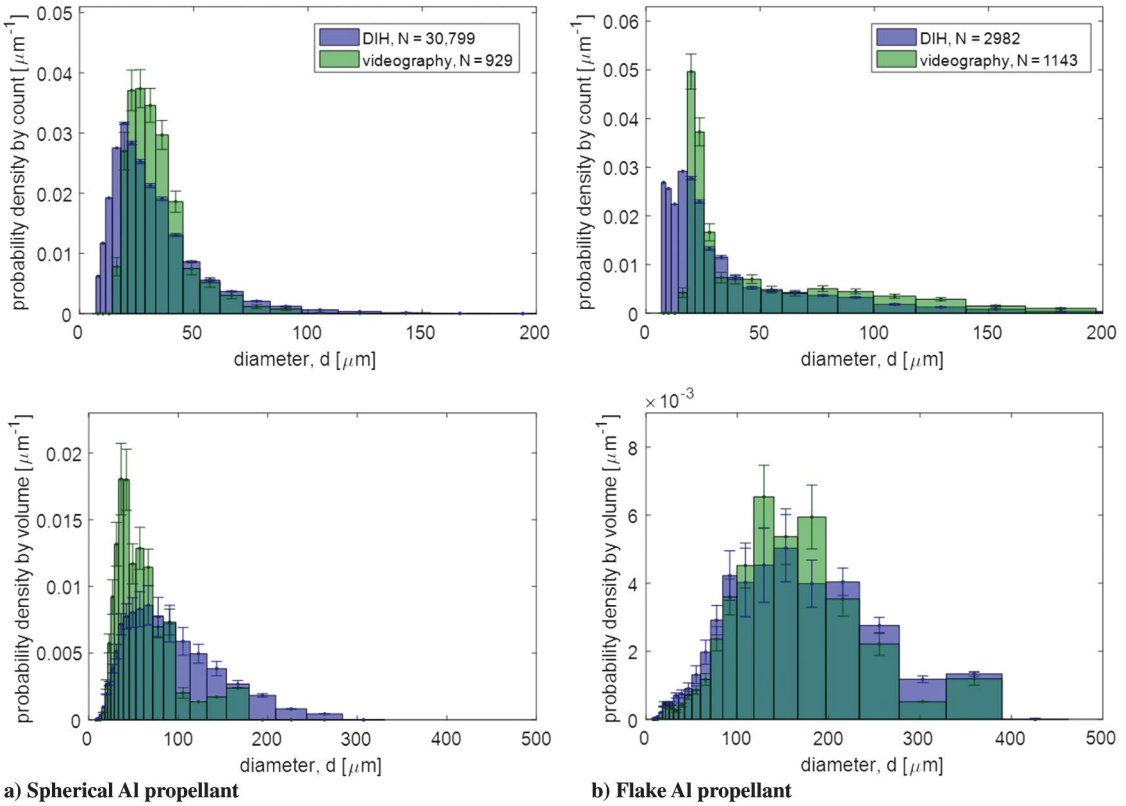

a) Spherical Al propellant **b) Flake Al propellant**

Fig. 12 Probability densities quantified by videography and DIH (4 Hz, size–velocity corrected results from Fig. 9).

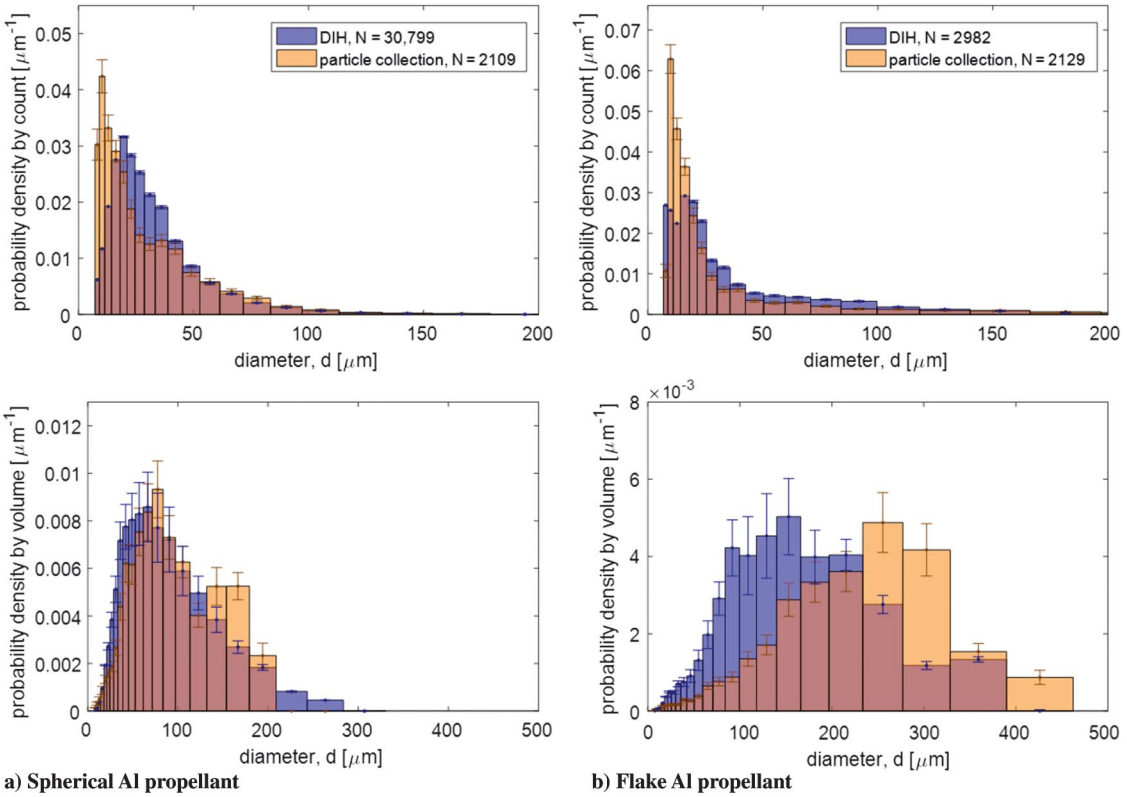

a) Spherical Al propellant **b) Flake Al propellant**

Fig. 13 Probability densities quantified by particle collection and DIH (4 Hz, size–velocity corrected results from Fig. 9).

techniques reported in the literature should be done with extreme caution.

Figure 12 specifically compares the probability densities measured by DIH in blue and videography in green. Overall, the results appear to agree relatively well. This outcome is perhaps not surprising, given that both techniques are based on imaging the particles in flight and sizing them using relatively similar image-processing techniques. Interestingly, it appears that the qualitative agreement in terms of the number probability is better for the spherical Al (top left in Fig. 12) as compared to the flake Al (top right in Fig. 12). However, when plotted in terms of a volume probability, the situation is reversed, with flake Al (bottom right in Fig. 12) appearing to be in better agreement than spherical Al (bottom left in Fig. 12). The fact that DIH and videography results do not match well for spherical Al is likely a reflection of the large number of particles needed to fully quantify a volume-weighted distribution. For example, of all particles measured with videography for the spherical Al result, the maximum measured diameter is about 160 μm. In the DIH results, where significantly more particles are measured, only about 0.3% by count is greater than 160 μm. However, when weighted by volume, this small number of large particles contributes over 16% of the total measured particle volume. One likely reason that the videography results do not fully capture the tail of the volume distribution at larger diameters is due to the significantly lower number of total particles measured. Additional future work is needed to understand this discrepancy.

Figure 13 compares the probability densities measured by DIH in blue and particle collection in orange. Once again, the general trends appear to agree relatively well, although there are important specific differences. For both the spherical and flake Al propellants, the peak in the volume size distributions (bottom row) is larger for particle collection with respect to DIH. One potential reason for the discrepancy is that the particle density on the quench plate is high, and is therefore more likely to have multiple particles overlapping, leading to higher measured particle sizes. Another possible explanation is the tendency of large molten particles to expand into an oblate shape as their momentum impinges onto the quenching medium. Generally, larger particles will be more susceptible to this effect due to potentially higher momentum as well as reduced surface tension forces, which scale with surface curvature. This explanation is consistent with the observation that differences are much more pronounced for the flake Al, where agglomerate diameters are larger, more sintered, and likely more malleable due to their high-temperature flame zones. Spherical Al measurements show more similarity between DIH and particle collection methods where agglomerate diameters are smaller. Volumetric quenching in a bath may be one potential future method for reducing this effect.

To better quantify the observed trends, Tables 1 and 2 show characteristic diameters determined from the probability densities of DIH, particle collection, and videography. Table 1 summarizes the spherical Al results, whereas Table 2 considers the flake Al result. Many options exist to characterize a mean diameter from a multivalued distribution of particle sizes [44]. Here, a few typical characteristic diameters are reported. The first four rows in Tables 1 and 2 are defined by the following

$$D_{pq} = \left[\sum d^p / \sum d^q\right]^{1/(p-q)} \tag{2}$$

where p and q are given by the values of the subscripts in the tables, and d is the individual diameter measurements. For example,

$$D_{10} = \left[\sum d^1 / \sum d^0\right]^{1/(1-0)}$$

is the classical average diameter given by the sum of all measured diameters divided by the total number of measurements. Likewise,

$$D_{30} = \left[\sum d^3 / \sum d^0\right]^{1/3}$$

is the diameter of a particle for which the volume is equal to the average of particle volumes. D_{32} and D_{43} are higher-order mean diameters that are often found to be important characteristic diameters for combustion studies [39]. The remaining six rows in Tables 1 and 2 define the diameter at various cutoffs of the probability

Table 1 Characteristic mean diameters for the spherical aluminum propellant

Characteristic mean diameter	DIH, μm	Particle collection, μm	Videography, μm	Variation, %
D_{10}	39 (35)	43 (33)	35	11[a]
D_{30}	53 (50)	59 (52)	42	18[b]
D_{32}	74 (73)	81 (79)	52	24[b]
D_{43}	103 (103)	105 (104)	67	27[c]
10% cutoff by count	19 (14)	19 (10)	21	4[a]
50% cutoff by count	32 (29)	36 (24)	31	9[a]
90% cutoff by count	66 (62)	76 (67)	55	17[b]
10% cutoff by volume	40 (39)	46 (45)	31	20[b]
50% cutoff by volume	90 (90)	96 (96)	58	29[c]
90% cutoff by volume	186 (186)	169 (169)	121	24[b]

[a]Measured variations less than 15%.
[b]Measured variations less than 25%.
[c]Measured variations greater than 25%.

Table 2 Characteristic mean diameters for the flake aluminum propellant

Characteristic mean diameter	DIH, μm	Particle collection, μm	Videography, μm	Variation, %
D_{10}	58 (46)	72 (48)	64	12[a]
D_{30}	93 (84)	132 (111)	100	22[b]
D_{32}	143 (142)	217 (215)	145	29[c]
D_{43}	187 (187)	268 (267)	178	27[c]
10% cutoff by count	19 (11)	19 (10)	21	8%[a]
50% cutoff by count	38 (27)	39 (20)	42	6%[a]
90% cutoff by count	121 (106)	185 (134)	139	25[b]
10% cutoff by volume	86 (85)	142 (142)	95	32[c]
50% cutoff by volume	177 (176)	259 (259)	168	29[c]
90% cutoff by volume	313 (313)	429 (429)	270	27[c]

[a]Measured variations less than 15%.
[b]Measured variations less than 25%.
[c]Measured variations greater than 25%.

densities. For example, the 10% cutoff by count is that diameter for which 10% of all measured particles have a diameter smaller than this value. Similarly, the 10% cutoff by volume is that diameter for which 10% of the total measured volume consists of particles with diameters smaller than this value. For all characteristic diameters, the values reported for DIH have been corrected for size–velocity effects using the methods given in [43].

Many of these characteristic diameters are strongly affected by the minimum measurable particles size of each technique. In the present results, videography has the largest minimum diameter (16.5 μm), whereas DIH (6.3 μm) and particle collection (8.4 μm) allow for the measurement of significantly smaller particles. To remove these differences, the values reported for DIH and particle collection in Tables 1 and 2 have been calculated from all particles with measured $d > 16.5$ μm, whereas the values reported in parentheses are determined from all measured particles. As expected, those values that are most strongly affected by the minimum measurable diameter include quantities derived from the lower tail of the number probability density (10% cutoff and 50% cutoff by count) as well as the number mean diameter D_{10}. These results suggest that a comparison of results reported in the literature, where the minimum measurable diameter varies widely, should be done with caution.

The final column in Tables 1 and 2 shows the percent variation in the measured characteristic diameters between all three techniques. Specifically, this is defined as the maximum absolute difference between the measured value from each technique and the mean value from all three techniques normalized by the same mean. These results are all determined using the characteristic diameters determined with the consistent minimum cutoff diameter of 16.5 μm. To visualize the relative values, measured variations of less than 15%, are highlighted in green, less than 25% in yellow, and greater than 25% in red are denoted. Although far from a perfect comparison, if the measurements performed here are assumed to be approximately similar to results previously reported by others, the percent variation in Tables 1 and 2 can provide an approximation for expected confidence bounds of reported characteristic diameters. In general, the measured characteristic diameters with the least variation are the mean diameter by count D_{10} and the median diameter by count (50% cutoff by count). However, for most propellant combustion studies, particle volume distributions are of more interest than the particle number distribution. Unfortunately, the measured characteristic diameters weighted by volume tend to show much higher variation, which is often on the order of 30%.

A few specific comments are warranted with respect to Tables 1 and 2. As illustrated in the previous probability density comparison figures, the table also shows that spherical Al shows a better match between DIH and particle collection results, whereas flake Al shows a better match between DIH and videography results. In general, the characteristic diameters measured with DIH and videography tend to agree better when compared to the particle collection results, which are typically higher. This result is likely due to the aforementioned flattening of large particles on the quench plate during particle collection. In addition, Sippel et al. [9,10] reported the size distributions of the spherical and flake Al power diameters before combustion. For the spherical Al agglomerates measured after combustion in Table 1, almost all of the numerically weighted characteristic diameters fall within the 25–75 μm range of the initial constitute powder, whereas the volumetrically weighted diameters are significantly larger. This illustrates the importance of considering volumetrically weighted diameters to fully quantify the effects of particle agglomeration.

Finally, in addition to differing measurement biases, each technique considered here also has specific advantages and challenges with regard to measurement complexity and flexibility. Contrasted with direct imaging, particle collection requires an additional collection apparatus along with experimental postprocessing via microscope imaging. Furthermore, care is required to optimize the measurement time in order to collect sufficient particles for statistical analysis while ensuring the collected particle density does not show significant particle overlap. In addition, alumina smoke and other combustion products can condense onto the quench disk, as noticed by white outlines around some particles in Fig. 10a, and can interfere in particle recognition for sizing agglomerates.

This effect can be reduced by optimizing the height of the quench plate and its velocity; however, these parameters will also affect the measured physical quantity. Finally, without direct flame imaging, particle collection provides little insight into particle combustion or burning surface phenomena. Ideally, the best use for particle collection is for measurements at high pressure, where optical- and laser-based techniques are more difficult to perform.

Compared with particle collection, direct imaging techniques, including videography and DIH as studied here, are relative easy to set up, with DIH being more complex due to the use of a collimated laser beam. A particular advantage of direct imaging is the ability to plot measured results onto the raw image, such as in Figs. 4–6 and 11. With this, the measurement quality can be directly visualized. Furthermore, these techniques can image particle combustion and burning surface phenomena. However, compared to particle collection, equipment costs are significantly higher, particularly when performing high-speed imaging. In addition, image processing for automatic extraction of results relies on customized algorithms, which are not widely available and, in the case of DIH, require significant computational resources. Finally, and perhaps most important for rocket motor applications, direct imaging is difficult at conditions approaching rocket motor pressures where the flowfield becomes optically dense [45]. For example, we attempted initial DIH experiments in an optically accessible combustion chamber at ~2.0 MPa. The resulting images appeared to be severely affected by signal absorption as well as beam steering, such that clear refocused images, analogous to Fig. 3, could not be obtained.

Overall, the results in this section indicate that many measurement techniques can provide quantification of particle size distributions. However, measurement biases and uncertainty may be high. Here, we have attempted to understand some of these uncertainties. Nevertheless, due to the complexity of each technique as well as the challenging measurement environment, full quantification of all biases and uncertainties is not yet possible and much work remains. The results here suggest that simultaneous use of multiple measurement techniques can provide useful checks on data quality. Particularly when pursuing accurate results at high pressure where measurements are mostly limited to particle collection, it may be best to perform initial low-pressure experiments, including using a combination of techniques to first verify accuracy.

V. Conclusions

This work presents an experimental comparison of three different particle sizing techniques for quantification of agglomerate size distributions formed during the combustion of aluminized ammonium perchlorate composite propellants. Particle collection on a quench medium and direct imaging of the in-flight agglomerates are two relatively common techniques found in the literature. In addition, this work also employs digital in-line holography, which is an emerging laser-based technique for 3-D imaging of the in situ agglomerates. Two different propellant formulations are considered: one consisting of aluminum (Al) particles with initial spherical morphology, as is common in current solid rocket applications; and a second using Al particles with an initial flakelike morphology.

Experimental results demonstrate that all three measurement techniques resolve the underlying quantitative trends. For example, all results show increased mean agglomerate sizes as compared to the initial, unreacted Al constitutes. Furthermore, mean agglomerate sizes from the flake Al are larger as compared to the spherical Al, indicating that initial particle morphology plays a large role in agglomeration dynamics. On the other hand, quantitative results show some notable differences. The particle size distributions measured by videography and digital inline holography (DIH) are similar, whereas the mean particle size measured with particle collection tends to be higher. It is theorized that particle collection suffers from a bias wherein the molten drops expand upon impact on the quench plate resulting in higher apparent measured diameters. Slight variations between propellant strands from the same batch and small discrepancies in the collection heights above the propellant between the techniques may also contribute to the observed differences.

The minimum measurable particle diameters of each technique are shown to strongly affect the measured mean diameters. Thus, various characteristic mean diameters are reported and compared. Up to a 30% variation in the results is observed between the three techniques, particularly for the characteristic diameters weighted by droplet volumes. Overall, these results indicate that care should be applied when making quantitative comparisons of droplet size distributions from the varied literature results, which typically only use a single measurement technique.

Imaging results that quantify particles within a measurement volume at discrete instants can be subject to size–velocity correlation biases. For example, the low-speed DIH results reported here are shown to oversample large particles that are relatively slow as compared to the smaller particles. These effects are removed by quantifying the mean particle velocities as a function of size using a second high-speed DIH recording. By combining data from the high-speed recording, which has relatively good temporal resolution, with a low-speed recording, which has relatively good spatial resolution, this work demonstrates new techniques to quantify the underlying size distribution over an enhanced size dynamic range while removing the size–velocity correlation biases.

Finally, benefits and drawbacks exist for each technique. Particle collection is intrusive and requires an additional experimental apparatus and postprocessing. On the other hand, it can be employed at high pressures where the optical density of the plume prevents reliable imaging results. Direct imaging of the in-flight particles with techniques such as videography and DIH uses comparatively simple experimental setups and can provide additional details of particle trajectories and combustion. Direct backlit videography is the simplest setup, but it can only quantify those particles within the relatively narrow depth of field of the high-magnification optics. On the other hand, DIH greatly extends the measurement depth via numerical refocusing. However, to achieve this, the postprocessing of DIH is significantly more complex and currently requires highly customized algorithms.

Due to the challenges of obtaining accurate measurements in this complex, reacting multiphase environment, these results suggest that multiple independent measurement techniques should be employed when possible to check measurement biases and provide some understanding of uncertainties. For solid rocket motor applications, where measurements are desired at high pressure, direct imaging may be challenging due to the high optical densities. Therefore, it may be necessary to perform initial low-pressure experiments where both particle collection and imaging are viable before progressing to higher pressures. More work is also needed to better understand the limitations of imaging results at higher pressures. Laser-based DIH might be extendable to higher pressures with alternative wavelengths that display improved transmission through the propellant plume.

Acknowledgments

The portion of this work completed at Sandia National Laboratories was supported by the Laboratory Directed Research and Development program and the Weapons Systems Engineering Assessment Technology program. Sandia National Laboratories is a multimission laboratory that is managed and operated by National Technology and Engineering Solutions of Sandia, LLC, which is a wholly owned subsidiary of Honeywell International, Inc., for the U.S. Department of Energy's National Nuclear Security Administration under contract DE-NA0003525.

References

[1] Price, E. W., and Sigman, R. K., "Combustion of Aluminized Solid Propellants," *Solid Propellant Chemistry, Combustion, and Motor Interior Ballistics, Progress in Aeronautics and Astronautics*, Vol. 185, AIAA, Reston, VA, 1999, pp. 663–688.

[2] Geisler, R., "A Global View of the Use of Aluminum Fuel in Solid Rocket Motors," *38th AIAA/ASME/SAE/ASEE Joint Propulsion Conference and Exhibit*, AIAA Paper 2002-3748, July 2002, pp. 1–8. doi:10.2514/6.2002-3748

[3] Cheung, H., and Cohen, N. S., "Performance of Solid Propellants Containing Metal Additives," *AIAA Journal*, Vol. 3, No. 2, 1965, pp. 250–257. doi:10.2514/3.2838

[4] Sambamurthi, J. K., Price, E. W., and Sigman, R. K., "Aluminum Agglomeration in Solid-Propellant Combustion," *AIAA Journal*, Vol. 22, No. 8, 1984, pp. 1132–1138. doi:10.2514/3.48552

[5] Maggi, F., Bandera, A., Galfetti, L., De Luca, L. T., and Jackson, T. L., "Efficient Solid Rocket Propulsion for Access to Space," *Acta Astronautica*, Vol. 66, Nos. 11–12, 2010, pp. 1563–1573. doi:10.1016/j.actaastro.2009.10.012

[6] Babuk, V., Dolotkazin, I., Gamsov, A., Glebov, A., DeLuca, L. T., and Galfetti, L., "Nanoaluminum as a Solid Propellant Fuel," *Journal of Propulsion and Power*, Vol. 25, No. 2, 2009, pp. 482–489. doi:10.2514/1.36841

[7] Jayaraman, K., Chakravarthy, S. R., and Sarathi, R., "Quench Collection of Nano-Aluminium Agglomerates from Combustion of Sandwiches and Propellants," *Proceedings of the Combustion Institute*, Vol. 33, No. 2, 2011, pp. 1941–1947. doi:10.1016/j.proci.2010.06.047

[8] Galfetti, L., DeLuca, L. T., Severini, F., Colombo, G., Meda, L., and Marra, G., "Pre and Post-Burning Analysis of Nano-Aluminized Solid Rocket Propellants," *Aerospace Science and Technology*, Vol. 11, No. 1, 2007, pp. 26–32. doi:10.1016/j.ast.2006.08.005

[9] Sippel, T. R., Son, S. F., Groven, L. J., Zhang, S., and Dreizin, E. L., "Exploring Mechanisms for Agglomerate Reduction in Composite Solid Propellants with Polyethylene Inclusion Modified Aluminum," *Combustion and Flame*, Vol. 162, No. 3, 2015, pp. 846–854. doi:10.1016/j.combustflame.2014.08.013

[10] Sippel, T. R., Son, S. F., and Groven, L. J., "Aluminum Agglomeration Reduction in a Composite Propellant Using Tailored Al/PTFE Particles," *Combustion and Flame*, Vol. 161, No. 1, 2014, pp. 311–321. doi:10.1016/j.combustflame.2013.08.009

[11] Yetter, R. A., Risha, G. A., and Son, S. F., "Metal Particle Combustion and Nanotechnology," *Proceedings of the Combustion Institute*, Vol. 32, No. 2, 2009, pp. 1819–1838. doi:10.1016/j.proci.2008.08.013

[12] Bucher, P., Ernst, L., Dryer, F. L., Yetter, R. A., Parr, T. P., and Hanson-Parr, D. M., "Detailed Studies on the Flame Structure of Aluminum Particle Combustion," *Solid Propellant Chemistry, Combustion, and Motor Interior Ballistics*, Vol. 185, Progress in Aeronautics and Astronautics, AIAA, Reston, VA, 2000, pp. 689–722. doi:10.2514/5.9781600866562.0689.0722

[13] Cohen, N. S., "A Pocket Model for Aluminum Agglomeration in Composite Propellants," *AIAA Journal*, Vol. 21, No. 5, 1983, pp. 720–725. doi:10.2514/3.8139

[14] Maggi, F., Stafford, S., Jackson, T., and Buckmaster, J., "Nature of Packs Used in Propellant Modeling," *Physical Review E*, Vol. 77, No. 4, 2008, pp. 1–17. doi:10.1103/PhysRevE.77.046107

[15] Jackson, T. L., Najjar, F., and Buckmaster, J., "New Aluminum Agglomeration Models and Their Use in Solid-Propellant-Rocket Simulations," *Journal of Propulsion and Power*, Vol. 21, No. 5, 2005, pp. 925–936. doi:10.2514/1.11888

[16] Laredo, D., and Netzer, D. W., "Application of Optical Diagnostics to Particle Measurements in Solid Propellant Rocket Motors and Exhaust Plumes," *Particulate Science and Technology*, Vol. 11, Nos. 3–4, 1993, pp. 175–192. doi:10.1080/02726359308906633

[17] Laredo, D., McCrorie, J. I., Vaughn, J. K., and Netzer, D. W., "Motor and Plume Particle Size Measurements in Solid Propellant Micromotors," *Journal of Propulsion and Power*, Vol. 10, No. 3, 1994, pp. 410–418. doi:10.2514/3.23750

[18] Povinelli, L. A., and Rosenstein, R. A., "Alumina Size Distributions from High-Pressure Composite Solid-Propellant Combustion," *AIAA Journal*, Vol. 2, No. 10, 1964, pp. 1754–1760. doi:10.2514/3.2660

[19] Galfetti, L., DeLuca, L. T., Severini, F., Colombo, G., Meda, L., and Marra, G., "Pre and Post-Burning Analysis of Nano-Aluminized Solid Rocket Propellants," *Aerospace Science and Technology*, Vol. 11, No. 1, 2007, pp. 26–32. doi:10.1016/j.ast.2006.08.005

[20] Karasev, V. V., Onischuk, A. A., Glotov, O. G., Baklanov, A. M., Maryasov, A. G., Zarko, V. E., Panfilov, V. N., Levykin, A. I., and Sabelfeld, K. K., "Formation of Charged Aggregates of Al_2O_3 Nanoparticles by Combustion of Aluminum Droplets in Air," *Combustion and Flame*, Vol. 138, Nos. 1–2, 2004, pp. 40–54. doi:10.1016/j.combustflame.2004.04.001

[21] Melcher, J. C., Krier, H., and Burton, R. L., "Burning Aluminum Particles Inside a Laboratory-Scale Solid Rocket Motor," *Journal of Propulsion and Power*, Vol. 18, No. 3, 2002, pp. 631–640. doi:10.2514/2.5977-3947

[22] Cauty, F., Erades, C., and Desse, J. M., "Light Deviation Based Optical Techniques Applied to Solid Propellant Combustion," *Progress in Propulsion Physics*, Vol. 2, Oct. 2011, pp. 121–134. doi:10.1051/eucass/201102121

[23] Powers, J. P., and Netzer, D. W., "Automatic Particles Sizing from Rocket Motor Holograms," *Society of Photo-Optical Instrumentation Engineers (SPIE) Proceedings*, Vol. 1667, SPIE, San Jose, CA, May 1992, pp. 136–145. doi:10.1117/12.59628

[24] Walker, J. D., and Netzer, D. W., "Holographic Investigation of Metallized Solid Propellant Combustion in Two-Dimensional and Three-Dimensional Rocket Motors," M.S. Thesis, Naval Postgraduate School, Monterey CA, 1987.

[25] Butler, A. G., and Netzer, D. W., "Holographic Investigation of Solid Propellant Combustion," M.S. Thesis, Naval Postgraduate School, Monterey, CA, 1988.

[26] Faber, D. E., and Netzer, D. W., "Holographic Investigation of Solid Propellant Combustion Particulates," M.S. Thesis, Naval Postgraduate School, Monterey, CA, 1983.

[27] Guildenbecher, D. R., Cooper, M. A., and Sojka, P. E., "High-Speed (20 kHz) Digital In-Line Holography for Transient Particle Tracking and Sizing in Multiphase Flows," *Applied Optics*, Vol. 55, No. 11, 2016, pp. 2892–2903. doi:10.1364/AO.55.002892

[28] Chen, Y., Guildenbecher, D. R., Hoffmeister, K. N. G., Cooper, M. A., Stauffacher, H. L., Oliver, M. S., and Washburn, E. B., "Study of Aluminum Particle Combustion in Solid Propellant Plumes Using Digital In-Line Holography and Imaging Pyrometry," *Combustion and Flame*, Vol. 182, Aug. 2017, pp. 225–237. doi:10.1016/j.combustflame.2017.04.016

[29] Guildenbecher, D. R., Cooper, M. A., Gill, W., Stauffacher, H. L., Oliver, M. S., and Grasser, T. W., "Quantitative, Three-Dimensional Imaging of Aluminum Drop Combustion in Solid Propellant Plumes via Digital In-Line Holography," *Optics Letters*, Vol. 39, No. 17, 2014, pp. 5126–5129. doi:10.1364/OL.39.005126

[30] Babuk, V., "Study of Metal Agglomeration and Combustion," Final Rept. SPC 97-4033, Baltic State Technical Univ., St. Petersburg, Russia, 1996.

[31] Gany, A., and Caveny, L. H., "Agglomeration and Ignition Mechanism of Aluminum Particles in Solid Propellants," *Symposium (International) on Combustion*, Vol. 17, No. 1, 1979, pp. 1453–1461. doi:10.1016/S0082-0784(79)80137-X

[32] Glotov, O. G., Zarko, V. E., Karasev, V. V., and Beckstead, M. W., "Condensed Combustion Products of Metalized Propellants of Variable Formulation," *36th AIAA Aerospace Sciences Meeting and Exhibit*, AIAA Paper 1998-0449, 1998, pp. 2–7. doi:10.2514/6.1998-449

[33] Zepper, E. T., Pantoya, M. L., Bhattacharya, S., Marston, J. O., Neuber, A. A., and Heaps, R. J., "Peering Through the Flames: Imaging Techniques for Reacting Aluminum Powders," *Applied Optics*, Vol. 56, No. 9, 2017, pp. 2535–2541. doi:10.1364/AO.56.002535

[34] Gabor, D., "Holography, 1948–1971," *Proceedings of the IEEE*, Vol. 60, No. 6, 1972, pp. 655–668. doi:10.1109/PROC.1972.8725

[35] Katz, J., and Sheng, J., "Applications of Holography in Fluid Mechanics and Particle Dynamics," *Annual Review of Fluid Mechanics*, Vol. 42, No. 1, 2010, pp. 531–555. doi:10.1146/annurev-fluid-121108-145508

[36] Schnars, U., and Jueptner, W., *Digital Holography: Digital Hologram Recording, Numerical Reconstruction, and Related Techniques*, Springer, Berlin, 2005, pp. 41–69.

[37] Guildenbecher, D. R., Gao, J., Reu, P. L., and Chen, J., "Digital Holography Simulations and Experiments to Quantify the Accuracy of 3-D Particle Location and 2D Sizing Using a Proposed Hybrid Method," *Applied Optics*, Vol. 52, No. 16, 2013, pp. 3790–3801. doi:10.1364/AO.52.003790

[38] Gao, J., Guildenbecher, D. R., Reu, P. L., and Chen, J., "Uncertainty Characterization of Particle Depth Measurement Using Digital In-Line Holography and the Hybrid Method," *Optics Express*, Vol. 21, No. 22, 2013, pp. 26432–26449. doi:10.1364/OE.21.026432

[39] Gao, J., Guildenbecher, D. R., Engvall, L., Reu, P. L., and Chen, J., "Refinement of Particle Detection by the Hybrid Method in Digital In-Line Holography," *Applied Optics*, Vol. 53, No. 27, 2014, pp. G130–G138. doi:10.1364/AO.53.00G130

[40] Cai, W., Thakre, P., and Yang, V., "A Model of AP/HTPB Composite Propellant Combustion in Rocket-Motor Environments," *Combustion Science and Technology*, Vol. 180, No. 12, 2008, pp. 2143–2169. doi:10.1080/00102200802414915

[41] Lefebvre, A. H., *Atomization and Sprays*, Hemisphere, New York, 1989, pp. 79–102.

[42] Jackson, T. L., "Modeling of Heterogeneous Propellant Combustion: A Survey," *AIAA Journal*, Vol. 50, No. 5, 2012, pp. 993–1006. doi:10.2514/1.J051585

[43] Chen, Y., and Guildenbecher, D. R., "Quantitative, Bias-Corrected Measurements of Droplet Position, Size and Velocity with Digital In-line Holography," *ILASS-Americas 29th Annual Conference on Liquid Atomization and Spray Systems*, Inst. for Liquid Atomization and Spray Systems, Atlanta, GA, 2017.

[44] Alderliesten, M., "Mean Particle Diameters: From Statistical Definition to Physical Understanding," Ph.D. Dissertation, Delft Univ. of Technology, Delft, The Netherlands, 2008. doi:10.1081/BIP-200048774

[45] Pokhil, P., Logachev, V., and Mal'tsev, V., "Colaescence of Metal Particles During the Combustion of Metallized Ballistite Compositions and Fuel-Oxidized Mixtures," *Combustion, Explosion, and Shock Waves*, Vol. 6, No. 1, 1970, pp. 76–85. doi:10.1007/BF02044899

L. Maurice
Associate Editor